Electrochimica Acta 346 (2020) 136244

Contents lists available at ScienceDirect

Electrochimica Acta

journal homepage: www.elsevier.com/locate/electacta

Holey graphite: A promising anode material with ultrahigh storage for lithium-ion battery

Chen Yang [a, b, 1], Xiuying Zhang [a, 1], Jingzhen Li [a], Jiachen Ma [a], Linqiang Xu [a], Jie Yang [a], Shiqi Liu [a], Shibo Fang [a], Ying Li [a], Xiaotian Sun [c], Xiaoyu Yang [d], Feng Pan [e], Jing Lu [a, b, f, g, *], Dapeng Yu [a, b, h]

[a] State Key Laboratory for Mesoscopic Physics and Department of Physics, Peking University, Beijing, 100871, PR China
[b] Academy for Advanced Interdisciplinary Studies, Peking University, Beijing, 100871, PR China
[c] College of Chemistry and Chemical Engineering, Henan Key Laboratory of Function- Oriented Porous Materials, Luoyang Normal University, Luoyang, 471934, PR China
[d] Computer Network Information Centre, Chinese Academy of Sciences, Beijing, 100871, PR China
[e] School of Advanced Materials, Peking University, Shenzhen Graduate School, Shenzhen, 518055, PR China
[f] Collaborative Innovation Center of Quantum Matter, Beijing, 100871, PR China
[g] Beijing Key Laboratory for Magnetoelectric Materials and Devices, Beijing, 100871, PR China
[h] Shenzhen Key Laboratory of Quantum Science and Engineering, Shenzhen, 518055, PR China

ARTICLE INFO

Article history:
Received 7 February 2020
Received in revised form
15 March 2020
Accepted 13 April 2020
Available online 17 April 2020

Keywords:
Holey graphite
Rechargeable lithium-ion battery
Anode material
Ab initio calculations

ABSTRACT

Recently, the 2019 Nobel prize in chemistry awards to three pioneers in the lithium-ion batteries (LIBs). However, the most commercially used anode for LIBs is still graphite, which suffers from the limited Li-ion storage of 372 mAh/g. To improve the performance of the intrinsic graphite anode (IGA), we use the *ab initio* calculations to examine the holey graphite anodes (HGAs) with three hole densities (35%: HGA35, 46%: HGA46 and 61%: HGA61) for LIBs. Remarkably, the maximum Li-ion storages of HGAs are up to 714–1689 mAh/g, which are about 2–4.5 times as high as that of the IGA (372 mAh/g). Besides, the in-plane diffusion barrier for Li-ions is also reduced from 0.57 eV (IGA) to 0.35–0.42 eV (HGAs), suggesting a higher Li-ion diffusion rate. The holey structures could open an extra out-plane Li-ions diffusing channel with only one-fifth of the diffusion barrier of that in the IGA, implying an accelerated charge/discharge process in the applications. We also demonstrate the relatively small surface area change ratio of less than 3%–14% in the HGAs upon adsorption of the maximum Li concentration. Therefore, the holey structure is a promising strategy to improve the graphite anode for LIBs significantly.

© 2020 Elsevier Ltd. All rights reserved.

1. Introduction

Lithium-ion batteries (LIBs) have achieved great success since they were firstly commercialized by Sony Corporation in 1991 [1–4]. Recently, the 2019 Nobel prize in chemistry awarded to John B. Goodenough, M. Stanley Whittingham, and Akira Yoshino, who are pioneers in LIBs. From personal computers to electric vehicles, LIBs now play a more and more critical role in today's life. To meet the increasing demand for the power supply, it becomes urgent to improve the Li-ion storage of LIBs [5–7]. Up to now, graphite is still the most commercially used material as anode for LIBs. Nevertheless, there is a widely accepted notion that every six carbon atoms in the graphite hold only one Li-ion for each layer at most and form the LiC_6 structure [8–11], which limits the Li-ion storage of 372 mAh/g for the intrinsic graphite anode (IGA).

Many works have demonstrated that the modified graphite is a promising method to improve the Li-ion storage of the IGA. For instance, the graphite modified by nano-metallic-oxide (NMO-G) has a larger distance of the graphite layers and the increased degree of the structural disorder. These characters of the NMO-G provide a wider space for Li-ion storage, resulting in the high Li-ion storage of 675.9 mAh/g in the experiment [12]. Besides, the reduced graphite oxide (r-GO) inherits the layer structure of graphite but has a larger distance of the graphite layer of 3.74 Å (instead of 3.35 Å like the IGA [10,13]), and thus a wider space for Li-ion storage is generated

* Corresponding author. State Key Laboratory for Mesoscopic Physics and Department of Physics, Peking University, Beijing, 100871, PR China.
E-mail address: jinglu@pku.edu.cn (J. Lu).
[1] These authors contributed equally to this work.

https://doi.org/10.1016/j.electacta.2020.136244
0013-4686/© 2020 Elsevier Ltd. All rights reserved.

[13]. As a result, the Li-ion storage is improved up to 917 mAh/g for r-GO in the experiment [13]. Other modified structures like the fluoridized graphite anode [14], aluminum-modified r-GO anode [15] and the metallic oxide/R-GO compounds anode [16–18] also improve the Li-ion storage with similar mechanisms.

Another feasible method is to reduce the dimension of graphite and generate two-dimensional graphene anodes (2DGAs) [19]. 2DGAs have a higher surface area ratio and vast ion-occupation sites for Li-ions compared with the bulk IGA [19,20]. The previous study demonstrates that 2DGAs can generate higher Li-ion storage of 460 mAh/g in the experiment [21]. Besides, the modified 2DGAs can also get better performance for LIBs. For instance, the functionalized 2DGAs (by epoxy and hydroxyl) present high Li-ion storage of ~860 mAh/g in theory due to the formation of covalent Li–O bonds [22,23]. Disordered 2DGAs possess high Li-ion storage in the range of 794–1054 mAh/g in the experiment [24], which is mainly ascribed to the additional reversible storage sites such as edges and other defects. Besides, 2DGAs with the Stone-Wales defects can even achieve ultrahigh Li-ion storage of 1100 mAh/g in theory due to the enhanced charge transfer from Li-ions to the graphene substrate [25].

In addition to the methods above, the holey structure could be the third promising strategy to improve the performance of the IGA for LIBs [26]. Commonly, the interconnected holes help accommodate the structure deformation during the charge/discharge process, implying an enhanced the cycling stability [27]. More importantly, the holey structures could generate a wider space for ions storage, suggesting higher Li-ion storage [28]. Besides, the interconnected holes could facilitate the out-plane diffusion channels, which is particularly helpful to the LIBs performing at the accelerated charge/discharge process [29].

Motivated by the unique features of holey structures with such favorable properties, we use the first-principles calculations to examine the performance of the holey graphite anodes (HGAs) for LIBs. Three hole densities of HGAs (35%: HGA35, 46%: HGA46 and 61%: HGA61) are considered in our study. We firstly prove that the HGAs are thermodynamically stable at room temperature. After adsorbing Li-ions, the Fermi level of all these HGAs moves upward into the conduction band, which suggests the enhanced electrical conductivity of the HGAs. The in-plane diffusion barriers for single Li-ions are only 0.35–0.42 eV in the HGAs compared with that of 0.57 eV in the IGA, which means a higher Li-ion diffusion rate. We find the higher the hole density, the lower the in-plane diffusion barrier in the HGAs. The holey structure could also open an extra out-plane Li-ion diffusion channel with the diffusion barrier of 1.64 eV, which is only one-fifth of the diffusion barrier of Li-ions diffusing across one graphene layer of the IGA (8.23 eV). Such an extra channel probably accelerates the charge/discharge process of LIBs. The calculated Li-ions capacities of the HGAs can reach as high as 714–1689 mAh/g, with the HGA46 performing the highest. Such ultrahigh Li-ions capacities are about 2–4.5 times as high as that of the IGA (372 mAh/g). We also observed the appropriate average open-circuit voltages of about 0.64 and 0.86 V in the HGA35 and HGA46, respectively. More importantly, the HGAs show relatively small structure deformations upon adsorption of their maximum Li-ions concentrations with a superficial area change ratio of less than 3%–14%, implying good cycle stability. Hence, the holey structure is a promising strategy to improve the IGA for LIBs significantly.

2. Computational details

The structures of the HGAs and their Li-adsorbed compounds were fully optimized by the Vienna *Ab initio* Simulation Package (VASP) [30,31]. Additionally, the electronic properties (like the partial density of state, the charge density difference and Bader charge analysis [32]) were studied by the VASP due to its powerful functions in the electronic calculations. The climbing image nudged elastic band (CI-NEB) method was also implemented in the VASP transition state tools to calculate the diffusion barriers of Li-ions [33,34]. During the calculations, the weak van der Waals interaction was taken into consideration by using the DFT-D3 approach in the VASP, and the plane-wave basis set with the projector-augmented wave (PAW) pseudopotential were adopted [35,36].

The energies of the graphite interacted by alkali metal (Li/Na/K) had been calculated by the 'energy' codes in the Cambridge Sequential Total Energy Package (CASTEP) [37] in the previous study and were consistent with the experimental results [11]. Thus, we chose the CASTEP to calculate the energies of the HGAs and their Li-adsorbed compounds in our research for comparison. During the calculations, the weak van der Waals interaction was taken into consideration by using the DFT-D correction in the CASTEP, and the plane-wave basis set with the ultrasoft pseudopotential was adopted.

Quantum Atomistix ToolKit (ATK) 2019 was used to do the *ab initio* molecular dynamics (MD) simulations to test the thermodynamic stability of the HGAs [38]. Herein, we used the 2×2 supercells of the HGAs to do the MD simulations for more accurate results. The MD simulation was conducted in a canonical NVT ensemble with the 300 K Nose-Hoover thermostat, and the total MD time was 1500 fs. [39]. During the calculations, the weak van der Waals interaction was taken into consideration by using the DFT-D3 approach in the ATK, and the double-ζ plus polarization (DZP) basis with the FHI pseudopotential were adopted.

During the calculation in the VASP, CASTEP, ATK: the density functional theory (DFT) with a cutoff energy of 600 eV was used; the generalized gradient approximation (GGA) combined with the Perdew-Burke-Ernzerhof (PBE) form were adopted [40]; the *k*-point mesh was sampled by the Monkhorst–Pack method with a separation of 0.02 $Å^{-1}$; and the convergence thresholds of 10^{-6} eV for energy and 10^{-3} eV/Å for force were used.

3. Results and discussions

3.1. Structure and stability

Commonly, the intrinsic graphite has an AB-stack of the carbon layer structure in nature. However, many works have demonstrated that graphite with a certain intercalated concentration of Li shifts the stacking pattern to an AA-stack [9,10,41–43]. The graphene layers in an AA-stack has only 7 meV per atom higher energy than that of the AB-stack, but the AA-stack models dramatically simplify the research and also maintain the accuracy [44]. Thus, we start from a perfect AA-stack graphite and introduce a series of equilateral hexagonal holes to construct holey graphite models. Such a shape of the hole usually possesses better thermodynamic stability among the other shapes [45] and is easier to be fabricated in the experiment, as reported in the previous study [46]. Herein, all dangling bonds on the periphery of holes are suggested to be passivated by the hydrogen atoms in the calculation, according to the previous work [46,47].

The hole density R is defined by the equation:

$$R = \frac{S_{\mathrm{Hole}}}{S_{\mathrm{HGA}}} \tag{1}$$

where S_{Hole} and S_{HGA} are the areas of the hexagonal hydrogen passivated holes and the unit-cell of the holey graphite anodes (HGAs), respectively, as marked in Fig. 1 (a). We define the side length of the equilateral hexagonal hole as l, and the radius of the

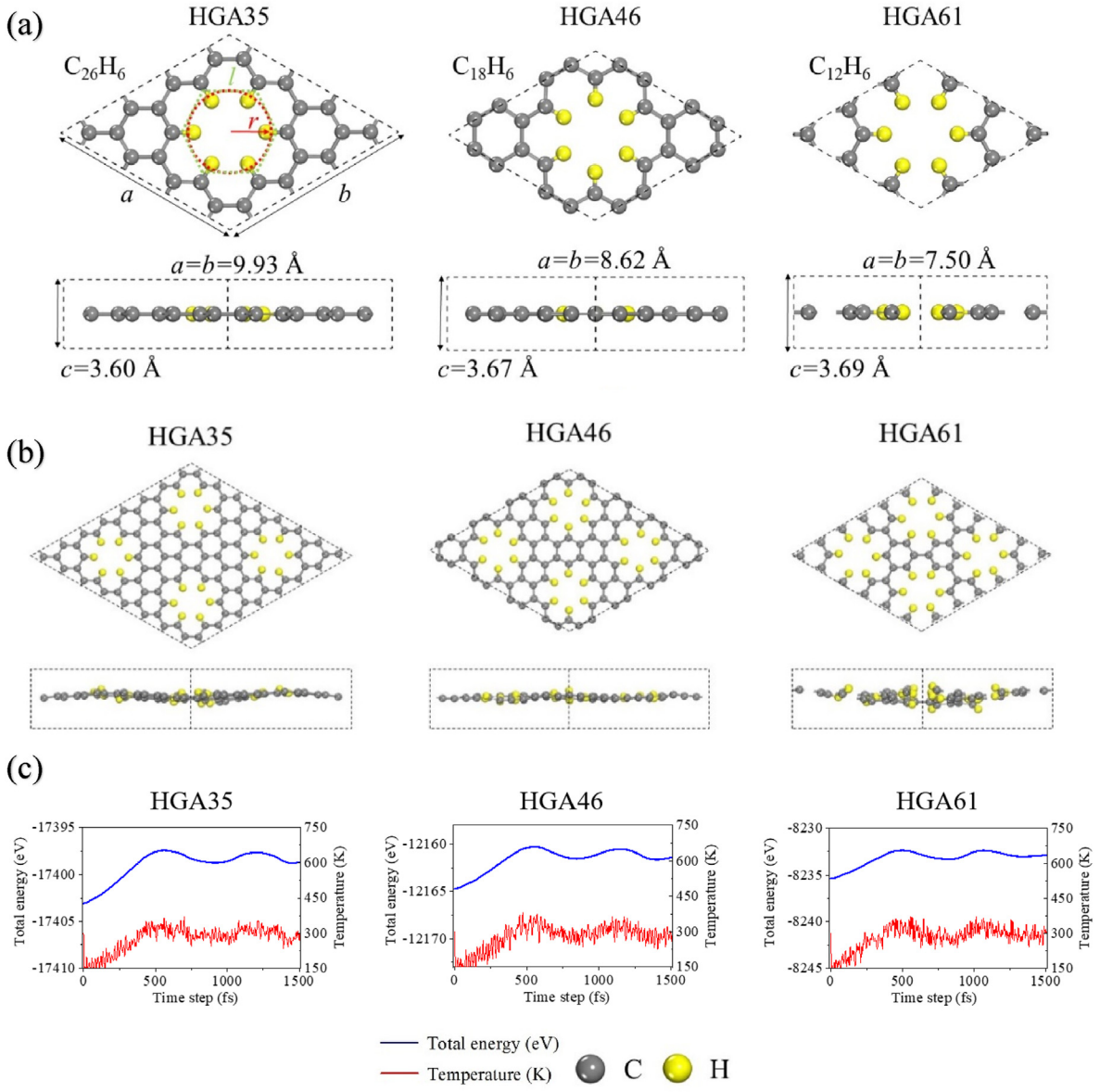

Fig. 1. (a) Optimized top and side views and lattice parameters of the HGA35, HGA46 and HGA61, respectively. The black dashed line means the unit cell of each holey graphite anode. The green dashed lines stand for the hexagonal hole, and the red dashed lines depict the tangent circle. (b) Top- and side-viewed snapshots of a relaxation event at 1500 fs of the 2 × 2 supercells of the HGA35, HGA46 and HGA61, respectively, in the MD simulations. (c) Total energies and temperatures of the 2 × 2 supercells of the HGA35, HGA46 and HGA61, respectively, during the 1500 fs of the MD simulations. (For interpretation of the references to color in this figure legend, the reader is referred to the Web version of this article.)

tangent circle is r. Mathematically, $l = \frac{2\sqrt{3}}{3}r$. Besides, a and b are defined as lattice parameters of the HGA unit-cell. For all the HGAs, c is the distance between the neighboring layers and set as 3.58 Å initially (the same as that of the AA-stack graphite) [44]. Thus, $S_{Hole} = \frac{3\sqrt{3}}{2}l^2$ and $S_{HGAs} = \frac{\sqrt{3}}{2}ab$, the hole density R could be calculated by the equation:

$$R = 4\frac{r^2}{ab} \tag{2}$$

By fixing the size of the hexagonal hydrogen passivated hole, different hole densities can be generated by varying the size of the unit-cell (the values of a and b) of the HGAs. As shown in Fig. 1 (a), we define three kinds of HGAs with the hole densities of R = 35% ($C_{26}H_6$), R = 46% ($C_{18}H_6$) and R = 61% ($C_{12}H_6$), respectively. These three HGAs are called HGA35, HGA46 and HGA61, respectively, in the following discussion.

After full optimizations, all the HGAs keep their initial structures, implying high statical stability. With the increasing hole density, the optimized c parameter increases to 3.60, 3.67 and 3.69 Å for the HGA35, HGA46 and HGA61, respectively in comparison with that of 3.58 Å for the AA-stack graphite. Thus, the holey structures could probably reduce the weak van der Waals interaction between the neighboring layers, resulting in a larger interlayer distance [48–50]. Moreover, thermodynamic stability is also crucial for the materials intended to use as an anode for LIBs. Here, we perform the *ab initio* molecular dynamics (MD) simulations to investigate the thermodynamic stability of the HGAs at room temperature. As shown in Fig. 1 (b), the HGA35 and the HGA46 kept the steady structure during 1500 fs with almost no deformation. As

for the HGA61, it presented a small amplitude in the *z*-direction at 1500 fs, implying a slight deformation. However, the HGA61 kept the steady structure in the *x*-*y* plane. The other snapshots of relaxation events at 500 and 1000 fs of the HGAs are shown in Fig. S1. Furthermore, the total energies and temperatures were balanced dynamically during the 1500 fs MD simulations for all the HGAs, as shown in Fig. 1 (c). From the above, we demonstrate the thermodynamic stability of the HGAs at room temperature [51,52].

3.2. Single Li atom adsorption

Then, the favorable adsorption sites should be found in the three HGAs for single Li atom. We find all the possible adsorption sites in consideration of the structure symmetry: the sites on the top of a carbon (C) atom or hydrogen (H) atom are marked as the numbers ('0' to '5') and at the center of the hexagonal rings are marked as the letters (E/H/Z) as shown in Fig. 2. Explicitly, we define the adsorption site at the hexagonal C—H ring (which is near the edge of the hexagonal hole) as the 'E' site, the center of the hexagonal hydrogen passivated hole as the 'H' site and the center of the hexagonal C—C ring (which is the nearest neighbor C—C ring to the hexagonal hole) as the 'Z' site. We try to adsorb one Li atom at every one of the adsorption sites, and these Li-adsorbed HGAs are going to get fully optimized. Following the previous work [53–61], the adsorption energy (E_{ad}) per Li atom is defined as:

$$E_{ad} = \frac{E_{Li_nHGA} - E_{HGA} - nE_{Li}}{n} \quad (3)$$

where E_{Li_nHGA}, E_{HGA}, and E_{Li} are the total energy of the Li-adsorbed HGAs, the pristine HGAs, and per Li atom in the metal lithium, respectively. And n is the number of Li atoms adsorbed in the HGAs. Under such a definition of the adsorption energy, E_{ad} should be negative when the HGAs have the ability to adsorb one Li atom. Besides, the larger absolute value of E_{ad} (in other words, the more negative of E_{ad}), the more stable Li-adsorbed HGAs [53–61].

Table 1 summarizes the calculated E_{ad} at the corresponding adsorption sites. For all the HGAs, the 'Z' sites are the most favorable adsorption sites for the Li atom with the E_{ad} of −1.62, −1.34 and −1.10 eV for the HGA35, HGA46 and HGA61, respectively. Such high absolute values of adsorption energies mean quite a steady adsorption, a rapid loading process and a significant potential for Li-storage application [5]. The structures of one Li atom adsorbed at the 'H' sites in the HGAs are all steady during the optimization. However, due to the positive values of these E_{ad}, all the 'H' sites cannot adsorb the Li atom under this condition. That means that hydrogen (H) atoms have no contribution to the Li-atom adsorption. Besides, all the 'E' sites possess the ability to adsorb Li atom, but the E_{ad} are not as strong as those of the corresponding 'Z' sites. It could be interpreted that the number of carbon atoms around the 'E' site is less than that of the 'Z' site, and then the adsorption ability would be weakened at the 'E' site relatively. In addition, the other adsorption sites are all unstable, and the Li atom moves to the nearby stable adsorption sites.

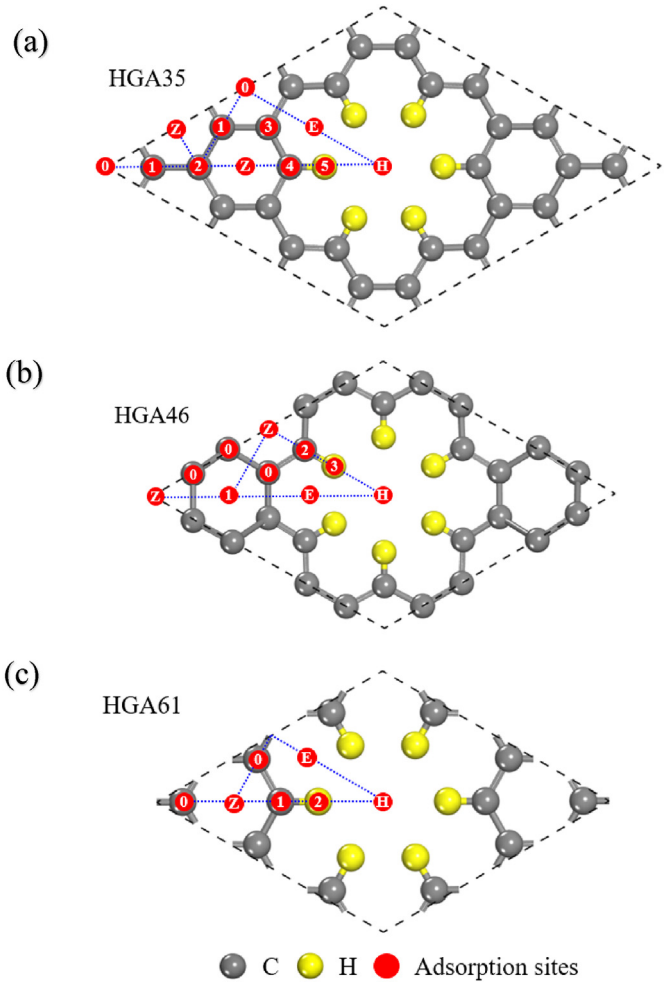

Fig. 2. Adsorption sites of Li-ions in the (a) HGA35 (b) HGA46 and (c) HGA61. The black dashed lines mean the unit cell of each holey graphite anode. The blue dashed sublines help find the symmetry of the HGAs. (For interpretation of the references to color in this figure legend, the reader is referred to the Web version of this article.)

3.3. Electronic property

Commonly, the electric conductivity of graphite would decrease after being constructed as the holey structures [46,47,62,63]. However, for the applications of anodes for LIBs, a good electrical conductivity is essential. In this section, we study the electronic properties of the Li-adsorbed HGAs.

The total density of states (TDOS) of the intrinsic HGAs and their Li-adsorbed structures (one Li atom adsorbed at the favorite 'Z' adsorption site) per unit-cell are illustrated in Fig. 3. Herein, the TDOS of the IGA and its maximum Li concentration adsorbed structure (LiC_6) are also calculated for comparison. The HGA35 keeps its good electric conductivity compared with the IGA. However, the HGA46 and HGA61 generate an energy gap of 0.20 and 0.88 eV around the Fermi level, respectively. That means the insulation of the hole structures will much influent the electric conductivity of the HGAs when the hole density is higher than (at least) 35%. Besides, we find that a higher hole density could generate a more significant energy gap, which accords with the previous study [46,62]. Remarkably, after the adsorption of the Li atom, the Fermi level of the Li-adsorbed HGAs moves upward into the conduction band. Thus, the Li adsorbed HGAs still possess the appropriate electric conductivities, which provides the enhancement for the applications of the Li adsorbed HGAs in LIBs. Besides, we found that the TDOS of the Li-adsorbed HGAs show no obvious difference to the HGAs with just the Fermi level moving into the conduction band. Such a phenomenon is similar to that of the Li adsorbed in the bulk Cu_3N [64], monolayer GaS [60], monolayer C_4N [51], and monolayer PC_6 [65]. As reported in these previous works, such a phenomenon indicates that the Li-atom adsorptions do not change the electronic properties of the HGAs, which implies that the dominating interaction between the Li-atoms and the HGA is ionic interaction instead of the covalent interaction.

Table 1
The adsorption energies at the different adsorption sites for the HGAs. Herein, the sites on the top of a carbon (C) atom or hydrogen (H) atom are marked as the numbers ('0' to '5') and at the center of a hexagonal ring are marked as the letters (E/H/Z) as shown in Fig. 3. Explicitly, we define the adsorption site at the hexagonal C—H ring (which is near the edge of the hexagonal hole) as the 'E' site, the center of the hexagonal hydrogen passivated hole as the 'H' site and the center of the hexagonal C—C ring (which is the nearest neighbor C—C ring to the hexagonal hole) as the 'Z' site. The arrows mean the adsorption site is changed after the optimization.

	Sites	0	1	2	3	4	5	E	H	Z
HGA35	E_{ad}(eV)	−1.55	→0	→Z	→E	→Z	→Z	−1.45	0.09	−1.62
HGA46	E_{ad}(eV)	→Z	−1.09	→Z	→Z	/	/	−1.23	0.44	−1.34
HGA61	E_{ad}(eV)	→Z	→Z	→Z	/	/	/	−1.06	0.29	−1.10

To get a further understanding of the interaction between the Li atom and HAGs, we studied the charge transfer phenomenon of the Li-adsorbed HGAs. Bader charge analysis indicates that Li atoms act as the electron donors and donate about $0.83e^-$, $0.84e^-$ and $0.84e^-$ per Li atom to the HGA35, HGA46, and HGA61, respectively. Such analyses mean that Li atoms exist in the ionic state in the Li-adsorbed HGAs.

Besides, the charge density difference ($\Delta\rho$) between the Li atoms and the HGAs is also calculated and displayed in Fig. 4. Herein, $\Delta\rho$ is defined as:

$$\Delta\rho = \rho_{Li-HGA} - \rho_{HGA} - \rho_{Li} \quad (4)$$

where ρ_{Li-HGA}, ρ_{HGA}, and ρ_{Li} represent the charge density values of the Li-adsorbed HGAs, the pristine HGAs, and a Li atom, respectively.

As a result, there is a net electron loss above the Li atom and a net electron gain between Li atoms and the nearby carbon atoms for all the HGAs. From the above, the results of the TDOS figures, the Bader charge analysis, and the charge density difference are entirely consistent. They indicate that there are electron transfers from the Li atoms to the HGAs, and the ionic interaction is formed between the Li-ions and the HGAs.

3.4. Diffusion barriers of single Li-ions

The in-plane diffusion pathway for single Li-ions diffusing in the IGA is shown in Fig. 5 (a), and a high in-plane diffusion barrier height of 0.57 eV is observed (in accordance with the previous reports [8,66,67]). The possible in-plane diffusion pathways and the corresponding energy profiles of the HGAs are shown in Fig. 5 (b)—(d). Each Li-ions starts from the favorite adsorption 'Z' sites, and then diffuses at the interlayer of the HGAs. Two in-plane diffusion pathways for Li-ions in the HGAs are considered in our study: (1) diffusing only at the residual carbon surface (named 'B-pathway') and (2) bypassing the edge of the hexagonal hydrogen passivated hole (named 'R-pathway'). Under such definitions, there are two possible in-plane diffusion pathways for the HGA35 and HGA46, respectively, but only 'R-pathway' for the HGA61.

The diffusion barrier heights along 'B-pathway' and 'R-pathway' are about 0.50 and 0.42 eV for the HGA35, respectively, and the corresponding diffusion lengths are 9.00 and 11.51 Å, respectively. The diffusion barrier heights along 'B-pathway' and 'R-pathway' are about 0.46 and 0.38 eV for HGA46, respectively, and the corresponding diffusion lengths are 5.31 and 5.48 Å, respectively. The diffusion length is longer for the 'R-pathway' than that of the 'B-pathway'. However, the diffusion barrier height is much smaller along the 'B-pathway' than along the 'R-pathway'. That could be interpreted as the reduced Li—C interactions around the edge of the hexagonal hydrogen passivated hole. Besides, for the HGA61, there is only the 'R-pathway' with the diffusion barrier height of 0.35 eV and the diffusion length of 5.57 Å. Remarkably, all the HGAs have a lower in-plane diffusion barrier height than that of IGA. Besides, the larger the hole density, the lower the in-plane diffusion barrier height. Those phenomena imply the holey structure could improve the Li-ions diffusion rate compared with the intrinsic graphite.

The holey structure could also open an extra out-plane diffusion channel for the Li-ions. The previous work has shown that the diffusion barrier of a given ion passing the hole on the graphene sheet is only related to the hole size [46]. Thus, we only take the HGA35 as an example and calculate the out-plane diffusion barrier height of the Li-ions travel through a hexagonal hydrogen passivated hole in the HGA35 (Fig. 6 (a)). The out-plane diffusion barrier height for the Li-ions diffusing across the hollow site in a hexagonal C—C ring of IGA is also calculated for comparison (Fig. 6 (b)). The calculated out-plane diffusion barrier is just 1.64 eV for the HGA35, which is only one-fifth of the diffusion barrier of that for the IGA (8.23 eV). Thus, the Li-ions could diffuse across the hole in the HGAs much easier than in the IGA and probably accelerate the charge/discharge process of LIBs.

3.5. Maximum Li-ion storages

The holey structure of the HGAs generates a larger distance between the neighboring layers, which commonly means a wider space for Li-ion storage. In this section, we investigate whether such a wider space could generate higher Li-ion storage than that of the IGA.

The E_{ad} as a function of Li concentration in the different HGAs are calculated and shown in Fig. 7. The E_{ad} as a function of Li concentration in the IGA is also calculated for comparison (LiC_{18}, LiC_{12}, LiC_8, LiC_6 structures are considered). Our calculated E_{ad} of the IGA in different Li concentrations accord with the previous works [8—10]. For each HGA, E_{ad} is negative at the low Li concentration, which indicates that the Li-adsorbed HGAs are stable. As the concentration increases, the absolute value of E_{ad} becomes smaller due to the weaker electrostatic attractions between the HGA hosts and the Li cations and the enhanced Li—Li interactions [51,60,65]. Generally, by gradually increasing the concentration of the Li atoms (Li_nHGA) before the E_{ad} turns to a positive value, and then the maximum number of Li adsorption per unit-cell (n_{max}) of the HGAs are obtained.

The negative E_{ad} indicate that the Li-ions can be adsorbed stably instead of clustering to form Li metal in the HGAs. Besides, the absolute value of E_{ad} is much higher than that in the IGA at each the same Li-ion storage, implying that the holey strategy in the IGA makes more active sites for Li adsorption [68—70]. Finally, we find the E_{ad} keeps negative until $n_{max} = 18$ and 14 for the HGA35 and HGA46, respectively, and the structures of the HGA35 and HGA46 are quite steady under the maximum Li-ion storage ($Li_{18}C_{26}H_6$ and $Li_{14}C_{18}H_6$), as shown in Fig. 8(a) and (b). However, for the HGA61, when the Li concentration increases to $n = 5$, the deformation of the HGA61 is quite obvious, as shown in Fig. S2. That means that the HGA61 is not even statically stable under a Li concentration higher than $Li_5C_{12}H_6$, which is not secure for the applications of LIBs. It could be interpreted that the large hole density generates enormous damage to the stability of the C—C frames in the HGA61, leading to poor structure stability under a relatively high Li

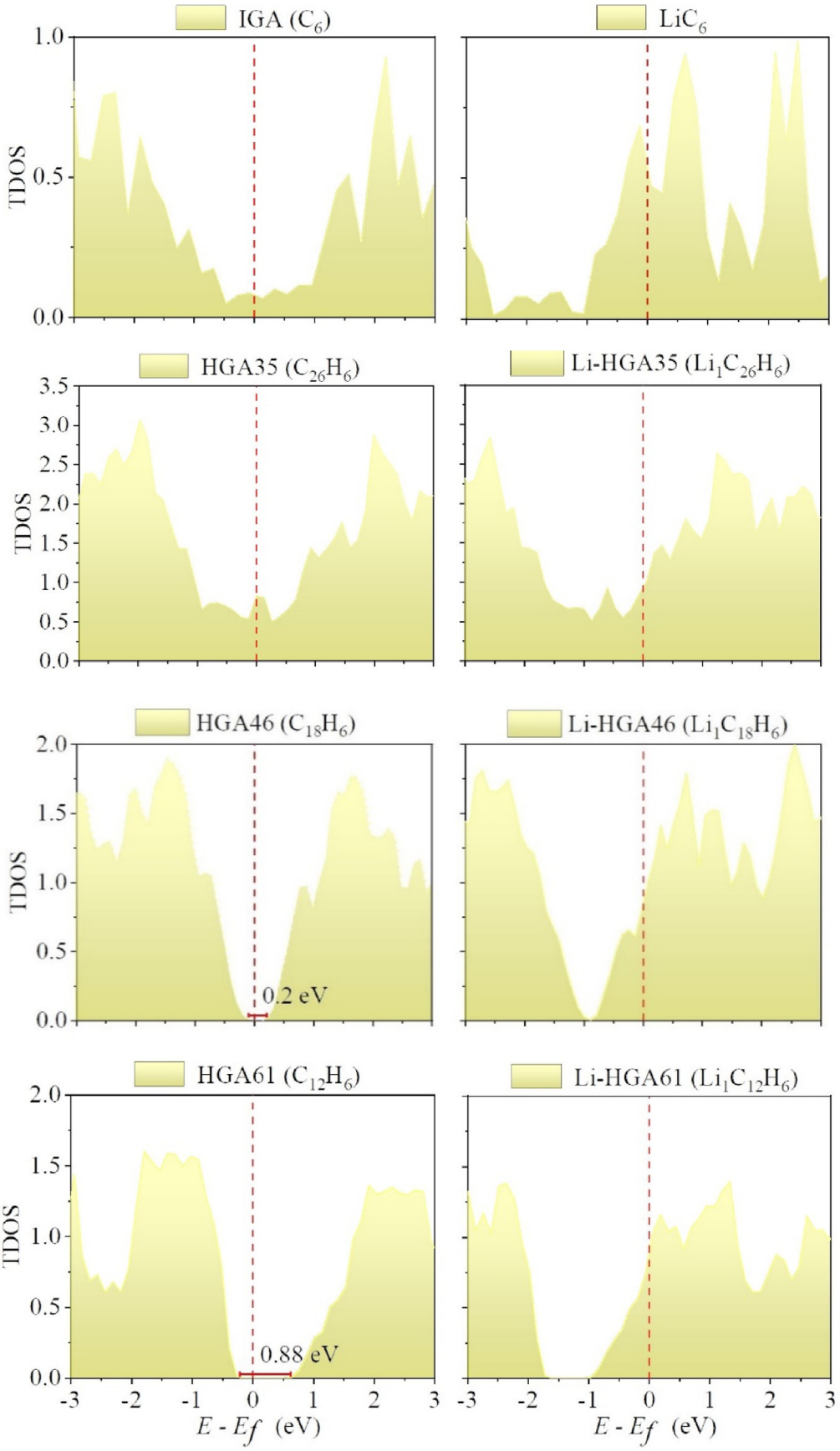

Fig. 3. Left: Total density of states (TDOS) of the IGA (C_6) and the intrinsic HGAs. Right: TDOS of the one Li adsorbed graphite (LiC_6) and HGAs. The red dashed line is the Fermi level, which is set to zero. (For interpretation of the references to color in this figure legend, the reader is referred to the Web version of this article.)

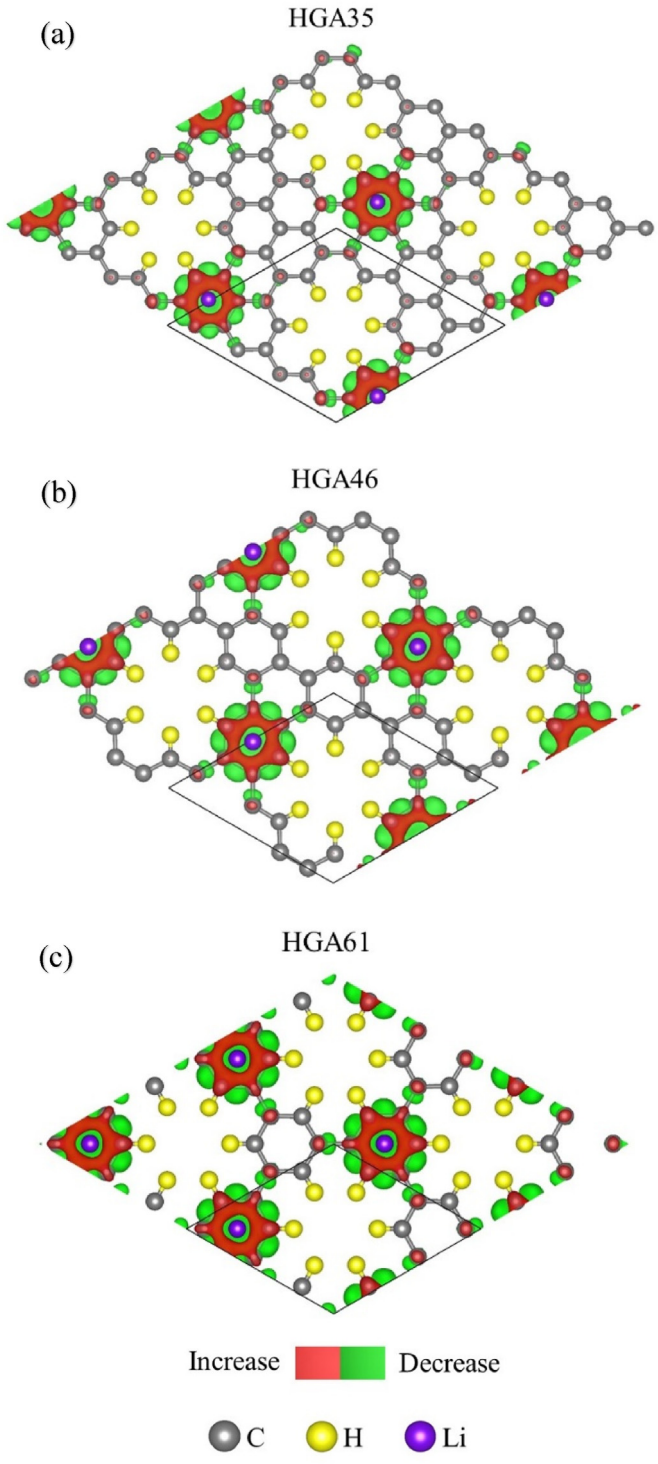

Fig. 4. Top views of difference charge density for one Li-ion adsorbed in (a) HGA35, (b) HGA46 and (c) HGA61. Red and green colors indicate the net increase and decrease of electrons. (For interpretation of the references to color in this figure legend, the reader is referred to the Web version of this article.)

concentration. Thus, the graphite with hole density below 46% is robust enough to keep the structure stability under a relatively high Li concentration. Besides, the structure of the HGA61 ($Li_4C_{12}H_6$) under a low Li concentration of $n = 4$ is also statically stable, as shown in Fig. 8 (c). Thus, the maximum Li concentration of the HGA61 is $n_{max} = 4$. The structures of the HGA35, HGA46 and HGA61 show little difference at the adsorption sites of the Li-ions when they both reach the maximum Li-ion storage, which has been discussed in the Supplementary Material.

The theoretical maximum Li-ion storage (C) for LIBs is determined by the maximum Li concentration (n_{max}) by the equation of [53–61].

$$C = \frac{1}{M} \times n_{max} \times F \quad (5)$$

where F is the Faraday constant (26801 mAh/mol), M is the atomic Molar weight per unit-cell (318.33, 222.25 and 150.18 g/mol for the HGA35, HGA46 and HGA61, respectively). For the IGA, considering the $M_{C_6} = 72.06$ g/mol and the corresponding $n_{max} = 1$, the maximum theoretical Li-ion storage is 372 mAh/g under such an equation [8–11].

The theoretical maximum Li-ion storages are 1516, 1689 and 714 mAh/g for the HGA35, HGA46, and HGA61, respectively, as shown in Fig. 9. Although the n_{max} of the HGA35 is higher than that of the HGA46, the larger M_{HGA} of the HGA35 leading to a relatively low Li-ion storage than the HGA46. The HGA61 has a relatively low Li-ion storage because of the low n_{max}. Remarkably, all these Li-ions capacities outdistance that of the IGA (372 mAh/g). The HGAs lead to a higher maximum Li/C ratio in comparison with that of the IGA. For the IGA, there is a widely accepted notion that the maximum Li/C is 0.17 (the LiC_6 structure). However, the maximum Li/C ratios are up to 0.69, 0.78 and 0.33, respectively, for the HGA35, HGA46 and HGA61. The much improved Li-ion storage is also observed in other holey carbonic anode materials. For instance, the monolayer nitrogenized holey graphene obtains ultrahigh Li-ion storage of 2939 mAh/g as the anode of LIBs in the first-principles study [71]. Such Li-ion storage outdistance that of 460 mAh/g in the perfect graphene anode [21]. Thus, the holey strategy is a feasible method to achieve higher Li-ion storage.

We calculate the electron localization functions (ELFs) for the HGAs with the maximum Li-ion storage, as shown in Fig. S3. Herein, we find that the electrons almost localize in the Li-ions or the HGAs substrate. Besides, there are always regions with ELF~0 between Li-ions and the HGAs and between each Li-ions. These results suggest that Li-ions are keeping ionic state even under the high Li concentration instead of clustering to form Li metal. We also find that the holey structure is like an electron-exchanging channel connecting each layer of Li-ions (especially in the HGA35 and the HGA46). Such an electron-exchanging channel could reinforce the adsorption of Li-ions in the HGAs.

The holey structure could provide the electron-exchanging channel; however, we should state that the improved theoretical maximum Li-ion storage is not due to the Li-storage in the hole space. The cause that the hexagonal hydrogen passivated hole cannot adsorb the Li atoms is the positive value of E_{ad} at the center of the hexagonal hydrogen passivated hole (0.09, 0.44 and 0.29 eV for the HGA35, HGA46 and HGA61, respectively). Actually, the following two reasons contributing to the higher Li-ion storage for LIBs: (1) A larger distance (3.60, 3.67 and 3.69 Å for the HGA35, HGA46 and HGA61, respectively, in comparison with that of 3.58 Å for the IGA) between the neighboring layers generating a wider space for Li storage per unit-cell indeed leads to a bigger n_{max} ($n_{max} = 18$, 14 and 4 for the HGA35, HGA46 and HGA61 in a unit-cell, respectively). (2) The holey structure leads to a lower atomic Molar weight per unit-cell M_{HGA} (the atomic Molar weight of the HGA35, HGA46 and HGA61 are about 83%, 77% and 69% of that of the IGA in the same unit-cell size, respectively).

3.6. Open-circuit voltage

Finally, we test the Open-circuit voltage (OCV) and cycling

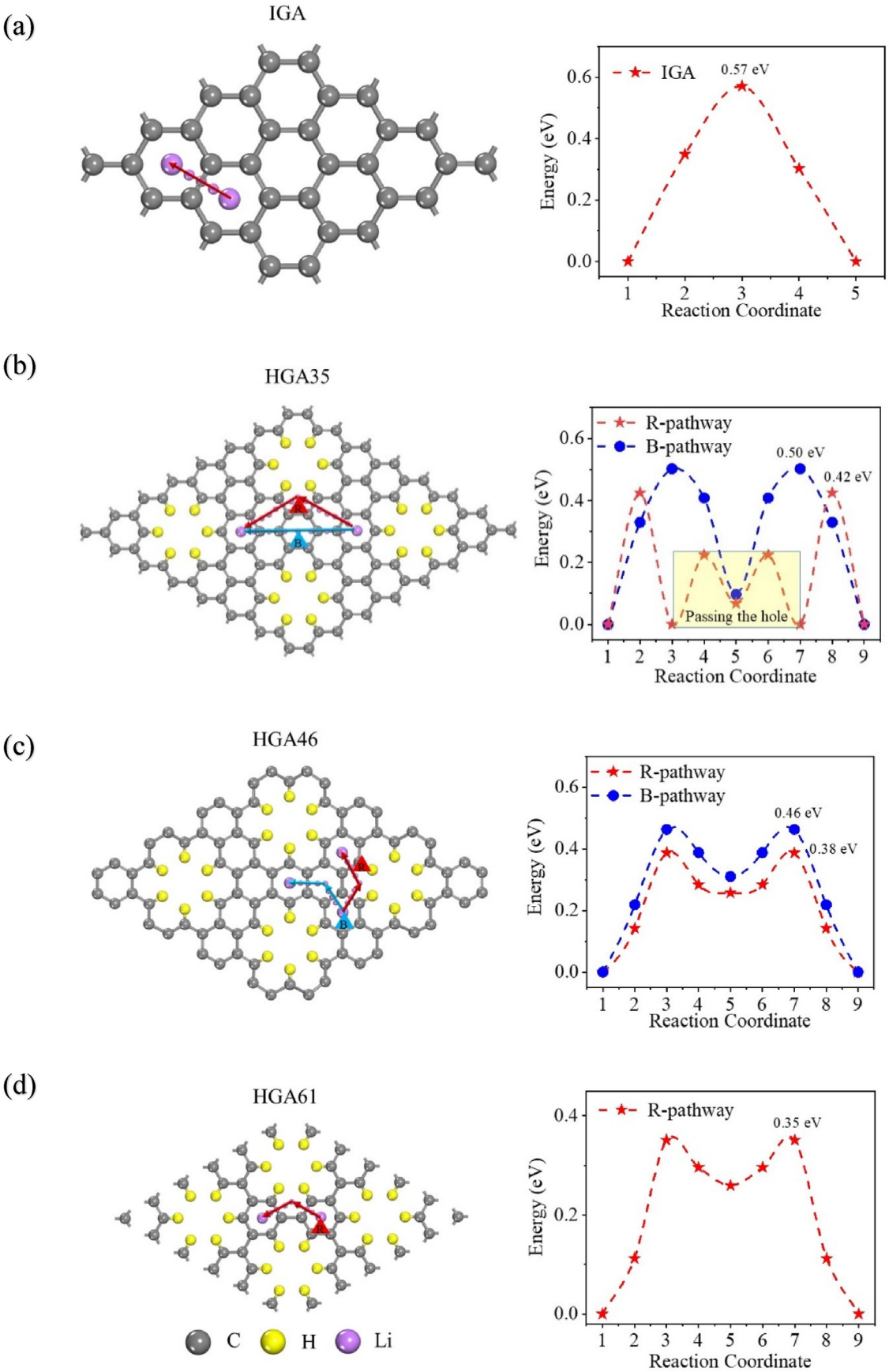

Fig. 5. In-plane diffusion pathways and energy profiles of Li-ions diffusing at the interlayer of the (a) IGA (b) HGA35 (c) HGA46 and (d) HGA61.

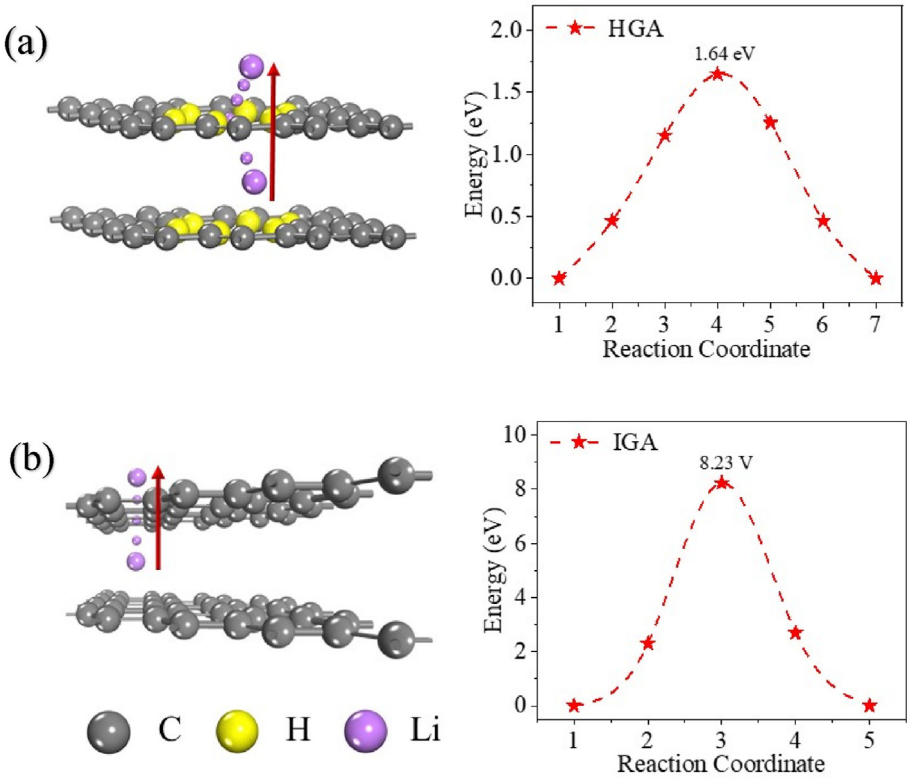

Fig. 6. (a) Out-plane diffusion pathway and energy profile of Li-ions through the hole of the HGA. (b) Out-plane diffusion pathway and energy profile of Li-ions through one layer of the IGA.

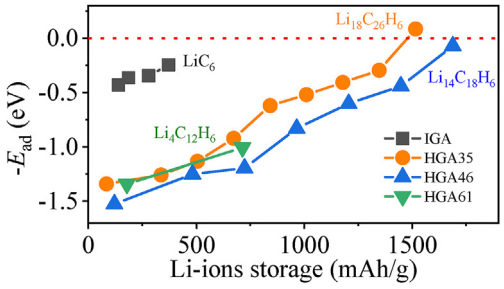

Fig. 7. Adsorption energy (E_{ad}) as a function of Li-ion storage in the IGA and HGAs.

stability of the HGAs which are crucial factors affecting the performance of LIBs. We can obtain the OCV curve by calculating the average voltage over the increasing values of the Li concentration. In theory, the charge/discharge process can be summarized as:

$$(n_2 - n_1)\mathrm{Li}^+ + (n_2 - n_1)\mathrm{e}^- + \mathrm{Li}_{n_1}\mathrm{HGA} \leftrightarrow \mathrm{Li}_{n_2}\mathrm{HGA} \quad (6)$$

When we neglect the pressure, volume and entropy effects, the average voltage of the HGAs in the concentration range of $n_1 < n < n_2$ can be calculated as [53–61].

$$\mathrm{V} \approx \frac{E_{\mathrm{Li}_{n_1}\mathrm{HGA}} - E_{\mathrm{Li}_{n_2}\mathrm{HGA}} + (n_2 - n_1)E_{\mathrm{Li}}}{(n_2 - n_1)\mathrm{e}^-} \quad (7)$$

where $E_{\mathrm{Li}_{n_1}\mathrm{HGA}}$ and $E_{\mathrm{Li}_{n_2}\mathrm{HGA}}$ are the total energy of Li_{n_1}HGA and Li_{n_2}HGA, E_{Li} is the average energy per Li atom in the metal lithium, n_1 and n_2 are the number of Li-ions adsorbed in the HGAs.

The voltage curves of three HGAs are presented in Fig. 10. Herein, we also present the voltage profile of the IGA for reference (comparing Li-adsorbed structure with the corresponding intrinsic structure). Commonly, there are three prominent voltage regions in the charging process of the anode: (1) plateau region corresponding to a weak interaction between the Li-ions at low Li concentration, (2) a region for increasing repulsive interaction between the Li ions, (3) a region for strong repulsive interaction where even a negative voltage is generated [72,73]. The first and second regions could be regarded as the reversible regions used as an anode for LIBs, which have been merged and marked orange, blue and green colors for the HGA35, HGA46 and HGA61 in Fig. 10, respectively. However, the gray third regions in Fig. 10(a) and (b) demonstrate the irreversible parts. Thus, the reversible Li-ion storages are 1010, 1205 and 714 mAh/g for the HGA35, HGA46 and HGA61, respectively, with the corresponding maximum Li concentration structure of $Li_{12}C_{26}H_6$, $Li_{10}C_{18}H_6$, and $Li_4C_{12}H_6$. The reversible Li-ion storage values of the HGA35 and HGA46 are only 67% and 71% of that of the corresponding maximum Li-ion storage values. However, they are still much larger than that of the most commercially used IGA of 372 mAh/g. We should state that the above reversible capacities are all based on the half-cell reaction (we only calculate the anode for the LIBs). When the HGAs are connected to a full-cell, the external voltage can overcome the repulsive interaction between Li-ions at high concentration and charge the HGAs to the theoretical maximum Li-ion storage.

We numerically average the voltage profiles and get the average OCV of about 0.64, 0.86 and 1.11 V for the HGA35, HGA46 and HGA61, respectively. These values are larger than that of IGA (0.11 V) [74], but much smaller than that of other widely studied anodes like TiO_2 (1.5–1.8 V) and black P (1.8–2.9 V) [75,76]. A lower OCV of the anode can guarantee a higher energy density and a high output voltage of the LIBs. However, a too low OCV for the anode would lead to a metal plating during the charge/discharge

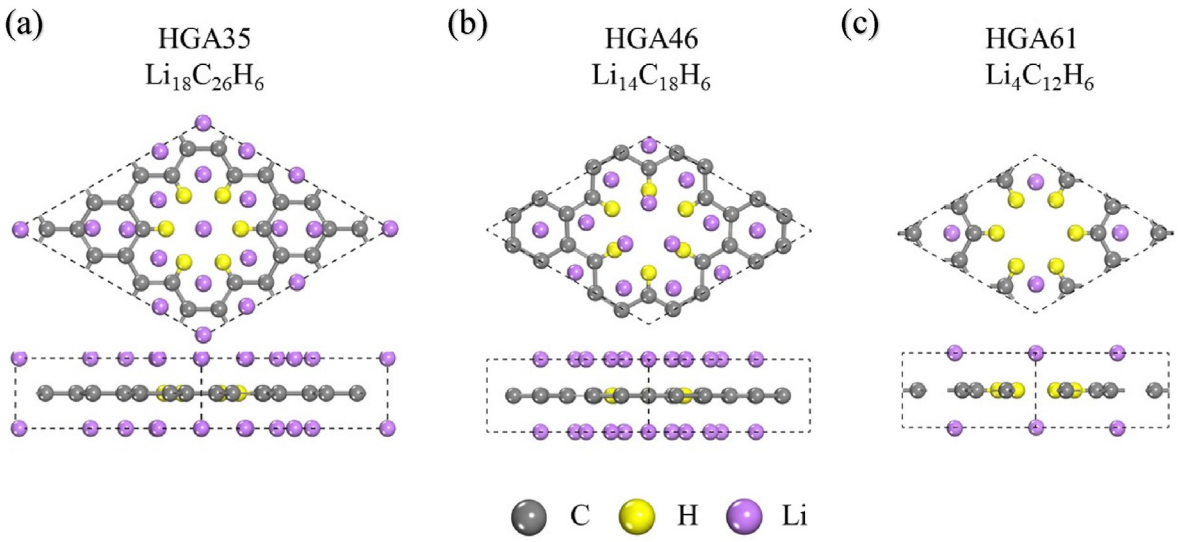

Fig. 8. Top and side views of the (a) HGA35 (b) HGA46 and (c) HGA61 adsorbed with the maximum Li-ion storage.

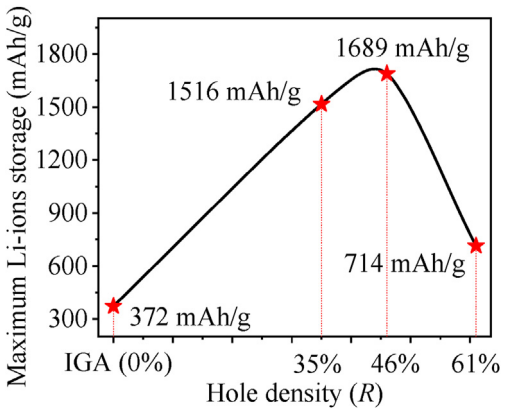

Fig. 9. Maximum Li-ion storage of HGAs as a function of the hole density. That of the IGA is also listed for comparison with the defined hole density of $R = 0\%$.

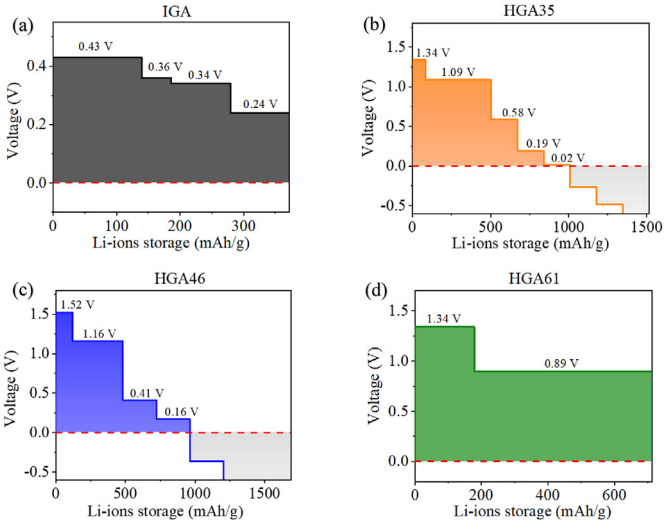

Fig. 10. Voltage profiles as a function of the Li-ion storage of the (a) IGA (comparing the Li-adsorbed structure with the corresponding intrinsic structure), (b) HGA35, (c) HGA46 and (d) HGA61. The reversible regions are marked orange, blue and green colors. The gray regions demonstrate the irreversible parts. (For interpretation of the references to color in this figure legend, the reader is referred to the Web version of this article.)

processing. Thus, the suitable OCV for an anode material is suggested in the range of 0.2–1.0 V [77]. Fortunately, the average OCV of the HGA35 and HGA46 are just in the suitable OCV range as the anode of LIBs. Thus, the HGA35 and HGA46 can be used as the anode of LIBs. By contrast, the average OCV of the HGA61 is a bit high to be used as the anode for LIBs.

3.7. Cycling stability

The cycle stability of the HGAs is also essential for LIBs, which is extremely sensitive to the structure deformation during the reversible charge/discharge process. It is known that significant surface area expansion might cause electrode pulverization and eventually lead to fast capacity fading and poor cycle stability [78]. Thus, we test the surface area expansion of the Li-adsorbed HGAs in this section (herein, that of the IGA is also presented for reference). Following the previous study, we define the surface area change ratio (ΔS) as [79].

$$\Delta S = [(S_{Li-HGA} - S_{HGA}) / S_{HGA}] \times 100\% \quad (8)$$

where S_{Li-HGA} and S_{HGA} are the surface area of the Li-adsorbed and pristine HGAs, respectively.

As plotted in Fig. 11, ΔS increases gradually with the increase of the Li concentration. Herein, the maximum ΔS are only 7.87%, 13.90% and 2.77%for the HAG35, HGA46 and HGA61, respectively, when they achieve the theoretical maximum Li-ion storages. Herein, the ΔS of the IGA adsorbed with its four Li-concentration structures (LiC_{18}, LiC_{12}, LiC_8, LiC_6) are also calculated for comparison. Obviously, at each of the same Li-ion storage, the superficial area change ratio of the IGA is much higher than those of the HGAs. Besides, they are much smaller than that of the silicon-based anode (400%) [78]. The low surface area change ratio of the HGAs may due to the holey structure accommodating the superficial area change, which also potentially slows down the cycle capacity fading of the HGAs during the charge/discharge process for better cycle stability [26]. Thus, the holey strategy is also a feasible method to achieve higher cycle stability for the IGA.

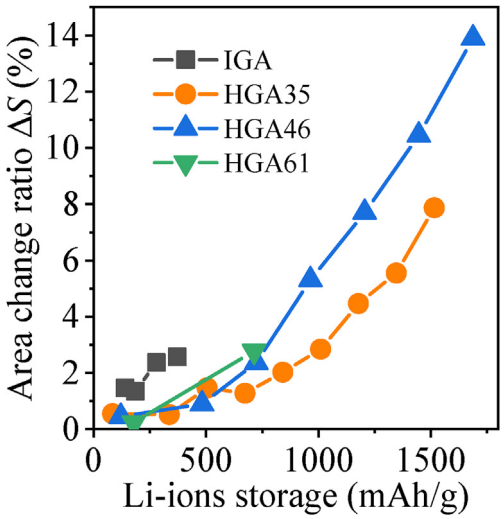

Fig. 11. Superficial area change ratio as a function of the Li-ion storage in the IGA and HGAs.

4. Discussion

The holey graphite performs well as the anode for LIBs and shows high stability according to our calculations. There is one question: how to realize the holey graphite structure in the real world? Actually, in 2010, Xiangfeng Duan's group has successfully created the so-called graphene nanomeshes (GNM) with the periodical and regular holey structure [80]. The graphene nanomeshes are prepared using block copolymer lithography and possess variable periodicities and neck widths as low as 5 nm. Besides, in 2019, Xiangfeng Duan's group has improved the pore size of the GNM to less than 1 nm by using O_2 plasma exposure [81]. Their methods can be used to create holey graphite anodes. In the previous study, the fabrication of regular two-dimensional carbon-based networks with single-atom wide holes and sub-nanometer periodicity has been realized by surface-assisted coupling of specifically designed molecular building blocks [63]. Thus, we believe that holey graphite anode is possible in the real world.

Besides, we demonstrate that the higher the hole density, the lower the in-plane diffusion barrier in the HGAs. The Li-ion capacity of the HGA46 is also higher than that of the HGA35, which means the higher the hole density, the larger the Li-ion capacity to some extent. On the other hand, the higher hole density would also bring a larger instability of material. For instance, the HGA61 presents a slight deformation in the z-direction compared with the steady structure of the HGA35 and HGA46 in MD simulations. Besides, the superficial area change ratio of the HGA46 is also higher than that of the HGA35. To generate the highest Li-ion storage, we suggest that the hole density of the HGAs should be closed to 46% in the experiment. However, to get less expansion and higher stability of the HGAs during the Li-ion charging process, the hole density of the HGAs should be closed to 35%.

5. Conclusion

In this paper, we used the first-principles calculations to examine the performance of the three kinds of HGAs with hole densities of 35% (HGA35), 46% (HGA46) and 61% (HGA61) as anodes for LIBs. We found that the HGAs possessed the following good characters: (1) the thermodynamic stability at room temperature, (2) the enhanced electrical conductivity in the single Li-adsorbed HGAs, (3) the lower in-plane diffusion barriers of 0.35–0.42 eV (which was much lower than that of 0.57 eV in the IGA), (4) an extra out-plane Li-ion diffusion channel with the diffusion barrier of 1.64 eV (which was only one-fifth of the diffusion barrier of 8.23 eV for Li-ion diffusing across one graphene layer of the graphite anode) (5) the ultrahigh Li-ion storages of 714–1689 mAh/g (about 2–4.5 times as high as that of the IGA), (6) an appropriate average OCV of about 0.64 and 0.86 V for the HGA35 and HGA46, (7) the relative small structure deformations of the HGAs upon adsorption of the maximum Li concentrations with the surface area change ratio of less than 3%–14%. Therefore, we indicated that the holey structure was a promising strategy to improve the IGA for LIBs.

Declaration of competing interest

The authors declare that they have no known competing financial interests or personal relationships that could have appeared to influence the work reported in this paper.

Acknowledgment

This work was supported by the Ministry of Science and Technology of China (No. 2016YFB0700600 (National Materials Genome Project) and 2017YFA206303), the National Natural Science Foundation of China (No. 11674005, 91964101, and 11664026), the High-performance Computing Platform of Peking University and the MatCloud + high throughput materials simulation engine.

Appendix A. Supplementary data

Supplementary data to this article can be found online at https://doi.org/10.1016/j.electacta.2020.136244.

References

[1] M.S. Whittingham, Electrical energy storage and intercalation chemistry, Science 192 (4244) (1976) 1126–1127.
[2] Yoshino, A.; Sanechika, K.; Nakajima, T., Secondary Battery. US Patent, 4668595, 1987-05-26.
[3] Y. Nishi, Lithium ion secondary batteries; past 10 Years and the future, J. Power Sources 100 (1–2) (2001) 101–106.
[4] Y. Lu, Q. Zhang, J. Chen, Recent progress on lithium-ion batteries with high electrochemical performance, Sci. China Chem. 62 (5) (2019) 533–548.
[5] A. Urban, D.H. Seo, G. Ceder, Computational understanding of Li-ion batteries, NPJ Comput. Mater. 2 (2016) 16002.
[6] M. Yoshio, R.J. Brodd, A. Kozawa, Lithium-Ion Batteries, Springer, New York, 2009.
[7] W.V. Schalkwijk, B. Scrosati, Advances in lithium ion batteries introduction, in: Advances in Lithium-Ion Batteries, Springer, Boston, MA, 2002, pp. 1–5.
[8] P. Ganesh, J. Kim, C. Park, M. Yoon, F.A. Reboredo, P.R. Kent, Binding and diffusion of lithium in graphite: quantum Monte Carlo benchmarks and validation of van der Waals density functional methods, J. Chem. Theor. Comput. 10 (12) (2014) 5318–5323.
[9] D. Guerard, A. Herold, Intercalation of lithium into graphite and other carbons, Carbon 13 (4) (1975) 337–345.
[10] K. Nobuhara, H. Nakayama, M. Nose, S. Nakanishi, H. Iba, First-principles study of alkali metal-graphite intercalation compounds, J. Power Sources 243 (2013) 585–587.
[11] W. Wan, H. Wang, Study on the first-principles calculations of graphite intercalated by alkali metal (Li, Na, K), Int. J. Electrochem. Sc. 10 (4) (2015) 3177–3184.
[12] Y. Xie, M. Naguib, V.N. Mochalin, M.W. Barsoum, Y. Gogotsi, X. Yu, K.W. Nam, X.Q. Yang, A.I. Kolesnikov, P.R. Kent, Role of surface structure on Li-ion energy storage capacity of two-dimensional transition-metal carbides, J. Am. Chem. Soc. 136 (2014) 6385–6394.
[13] S. Yige, T. Jie, Z. Kun, Y. Jinshi, L. Jing, Z.D. Ming, O. Kiyoshi, Q.L. Chang, Comparison of reduction products from graphite oxide and graphene oxide for anode applications in lithium-ion batteries and sodium-ion batteries, Nanoscale 9 (2017) 2585–2595.
[14] Q. Dong, Y. Zhu, M. Zheng, Y. Zhan, Z. Lin, Study on electrochemical

performance of fluorinated graphite and its application in alkaline batteries, J. Electrochem. Soc. 153 (2006) A459–A462.
[15] D. Wan, C. Yang, F. Huang, Low-temperature aluminum reduction of graphene oxide, electrical properties, surface wettability, and energy storage applications, ACS Nano 6 (2012) 9068–9078.
[16] Z. Guo, J. Wang, F. Wang, D. Zhou, Y. Wang, Y. Xia, Leaf-like graphene oxide with a carbon nanotube midrib and its application in energy storage devices, Adv. Funct. Mater. 23 (2013) 4840–4846.
[17] Y. Li, J. Qu, F. Gao, S. Lv, L. Shi, C. He, J. Sun, In situ fabrication of Mn_3O_4 decorated graphene oxide as a synergistic catalyst for degradation of methylene blue, Appl. Catal. B Environ. 162 (2015) 268–274.
[18] X. Zhu, Y. Zhu, S. Murali, M.D. Stoller, R.S. Ruoff, Nanostructured reduced graphene oxide/Fe_2O_3 composite as a high-performance anode material for lithium ion batteries, ACS Nano 5 (4) (2011) 3333–3338.
[19] X. Zhang, L. Hou, A. Ciesielski, P. Samorì, 2D materials beyond graphene for high-performance energy storage applications, Adv. Energy Mater. 6 (23) (2016) 1600671.
[20] W. Li, Y. Yang, G. Zhang, Y.-W. Zhang, Ultrafast and directional diffusion of lithium in phosphorene for high-performance lithium-ion battery, Nano Lett. 15 (2015) 1691–1697.
[21] G. Wang, X. Shen, J. Yao, J. Park, Graphene nanosheets for enhanced lithium storage in lithium ion batteries, Carbon 47 (8) (2009) 2049–2053.
[22] M.E. Stournara, V.B. Shenoy, Enhanced Li capacity at high lithiation potentials in graphene oxide, J. Power Sources 196 (13) (2011) 5697–5703.
[23] S.Y. Zhong, J. Shi, W.W. Luo, X.L. Lei, First-principles insight into Li and Na ion storage in graphene oxide, Chin. Phys. B 28 (7) (2019), 078201.
[24] D. Pan, S. Wang, B. Zhao, M. Wu, H. Zhang, Y. Wang, Z. Jiao, Li storage properties of disordered graphene nanosheets, Chem. Mater. 21 (14) (2009) 3136–3142.
[25] D. Datta, J. Li, N. Koratkar, V.B. Shenoy, Enhanced lithiation in defective graphene, Carbon 80 (2014) 305–310.
[26] L. Peng, Z. Fang, Y. Zhu, C. Yan, G. Yu, Holey 2D nanomaterials for electrochemical energy storage, Adv. Energy Mater. (2017) 1702179.
[27] B. Guo, X. Yu, X.G. Sun, M. Chi, Z.A. Qiao, J. Liu, Y.S. Hu, X.Q. Yang, J.B. Goodenough, S. Dai, A long-life lithium-ion battery with a highly porous $Tinb_2o_7$ anode for large-scale electrical energy storage, Energy Environ. Sci. 7 (2014) 2220–2226.
[28] Y. Ren, A.R. Armstrong, F. Jiao, P.G. Bruce, Influence of size on the rate of mesoporous electrodes for lithium batteries, J. Am. Chem. Soc. 132 (3) (2010) 996–1004.
[29] L. Peng, P. Xiong, L. Ma, Y. Yuan, Y. Zhu, D. Chen, X. Luo, J. Lu, K. Amine, G. Yu, Holey two-dimensional transition metal oxide nanosheets for efficient energy storage, Nat. Commun. 15139 (8) (2017), 2041-1723.
[30] G. Kresse, J. Hafner, Ab initiomolecular dynamics for liquid metals, Phys. Rev. B 47 (1993) 558.
[31] G. Kresse, J. Hafner, Ab initiomolecular-dynamics simulation of the liquid-metal–amorphous-semiconductor transition in germanium, Phys. Rev. B 49 (1994) 14251.
[32] W. Tang, E. Sanville, G. Henkelman, A grid-based bader analysis algorithm without lattice bias, J. Phys. Condens. Matter 21 (2009), 084204.
[33] G. Henkelman, H. Jónsson, A climbing image nudged elastic band method for finding saddle points and minimum energy paths, J. Chem. Phys. 113 (2000) 9901–9904.
[34] G. Henkelman, H. Jónsson, Improved tangent estimate in the nudged elastic band method for finding minimum energy paths and saddle points, J. Chem. Phys. 113 (2000) 9978–9985.
[35] P.E. Blochl, Projector augmented-wave method, Phys. Rev. B 50 (1994) 17953.
[36] G. Kresse, D. Joubert, From ultrasoft pseudopotentials to the projector augmented-wave method, Phys. Rev. B 59 (1999) 1758.
[37] S.J. Clark, M.D. Segall, C.J. Pickard, P.J. Hasnip, M.I.J. Probert, K. Refson, M.C. Payne, First principles methods using castep, Z. Kristallogr. 220 (2005) 567–570.
[38] Atomistix toolkit version 2019, quantumwise A/S (Copenhagen, Denmark), www.quantumwise.com.
[39] G.J. Martyna, M.L. Klein, M. Tuckerman, Nosé–hoover chains: the canonical ensemble via continuous dynamics, J. Chem. Phys. 97 (1992) 2635.
[40] J.P. Perdew, K. Burke, M. Ernzerhof, Generalized gradient approximation made simple, Phys. Rev. Lett. 78 (1997) 1396.
[41] K. Persson, Y. Hinuma, Y.S. Meng, A. Ven, G. Ceder, Thermodynamic and kinetic properties of the Li-graphite system from first-principles calculations, Phys. Rev. B 82 (12) (2010) 125416.
[42] G.C. Ri, C.J. Yu, J.S. Kim, S.N. Hong, U.G. Jong, M.H. Ri, First-principles study of ternary graphite compounds cointercalated with alkali atoms (Li, Na, and K) and alkylamines towards alkali ion battery applications, J. Power Sources 324 (2016) 758–765.
[43] K. Toyoura, Y. Koyama, A. Kuwabara, F. Oba, I. Anaka, First-principles approach to chemical diffusion of lithium atoms in a graphite intercalation compound, Phys. Rev. B 78 (21) (2008) 214303.
[44] Z. Wang, S.M. Selbach, T. Grande, Van Der Waals, Density functional study of the energetics of alkali metal intercalation in graphite, RSC Adv. 4 (8) (2014) 4069–4079.
[45] H. Jippo, M. Ohfuchi, C. Kaneta, Theoretical study on electron transport properties of graphene sheets with two- and one-dimensional periodic nanoholes, Phys. Rev. B 84 (2011), 075467.
[46] L. Liu, X. Yue, J. Zhao, Q. Cheng, J. Tang, Graphene antidot lattices as potential electrode materials for supercapacitors, Physica E 69 (2015) 316–321.
[47] X. Qin, Q. Meng, Y. Feng, Y. Gao, Graphene with line defect as a membrane for GaS separation: design via a first-principles modeling, Surf. Sci. 607 (1) (2013) 153–158.
[48] E. Hazrati, G. Wijs, G. Brocks, Li intercalation in graphite: a van der Waals density-functional study, Phys. Rev. B 90 (15) (2014) 155448.
[49] S. Grimmea, J. Antony, S. Ehrlich, H. Krieg, A consistent and accurate ab initio parametrization of density functional dispersion correction (DFT-D) for the 94 elements H-Pu, J. Chem. Phys. 132 (15) (2010) 154104.
[50] S. Grimme, S. Ehrlich, L. Goerigk, Effect of the damping function in dispersion corrected density functional theory, J. Comput. Chem. 32 (7) (2011) 1456–1465.
[51] C. Yang, et al., Ultrahigh capacity of monolayer dumbbell C_4N as a promising anode material for lithium-ion battery, J. Electrochem. Soc. 167 (2020), 020538.
[52] L. Xu, et al., Computational study of ohmic contact at bilayer InSe-metal interfaces: implications for field-effect transistors, ACS Appl. Nano Mater. 2 (11) (2019) 6898–6908.
[53] R. Bhandavat, L. David, G. Singh, Synthesis of surface-functionalized WS_2 nanosheets and performance as Li-ion battery anodes, J. Phys. Chem. Lett. 3 (2012) 1523–1530.
[54] M. Bohayra, D. Arezoo, R. Obaidur, C. Gianaurelio, R. Timon, Borophene as an anode material for Ca, Mg, Na or Li ion storage: a first-principle study, J. Power Sources 329 (2016) 456–461.
[55] D. Çakır, C. Sevik, O. Gülseren, F.M. Peeters, Mo_2C as a high capacity anode material: a first-principles study, J. Mater. Chem. A 4 (2016) 6029–6035.
[56] H.R. Jiang, Z.H. Lu, M.C. Wu, F. Ciucci, T.S. Zhao, Borophene: a promising anode material offering high specific capacity and high rate capability for lithium-ion batteries, Nanomater. Energy 23 (2016) 97–104.
[57] F. Li, Y.Y. Qu, M.W. Zhao, Germanium sulfide nanosheet: a universal anode material for alkali metal ion batteries, J. Mater. Chem. A 4 (2016) 8905–8912.
[58] J.C. Ma, J. Fu, M.Q. Niu, R.G. Quhe, MoO2 and graphene heterostructure as promising flexible anodes for lithium-ion batteries, Carbon (2019) 357.
[59] H.R. Jiang, W. Shyy, M. Liu, L. Wei, M.C. Wu, T.S. Zhao, Boron phosphide monolayer as a potential anode material for alkali metal-based batteries, J. Mater. Chem. A 5 (2017) 672–679.
[60] X.Y. Zhang, et al., Monolayer gas with high ion mobility and capacity as a promising anode battery, Material *J. Mater. Chem. A* 7 (2019) 14042–14050.
[61] Z.Z. Zhang, Y.F. Zhang, Y. Li, J. Lin, D.G. Truhlar, S.P. Huang, $MnSb_2S_4$ monolayer as an anode material for metal-ion batteries, Chem. Mater. 30 (2018) 3208–3214.
[62] Z. Liumin, K. Konishi, K. Yoh, Proposal of graphene bandgap control by hexagonal network formation, Jap. J. Appl. Phys. 50 (2011), 06GE14.
[63] M. Bieri, et al., Porous graphenes: two-dimensional polymer synthesis with atomic precision, Chem. Commun. 45 (2009) 6919.
[64] J. Wang, F. Li, X. Liu, H. Zhou, X. Shao, Y. Qu, M. Zhao, Cu_3n and its analogs: a new class of electrodes for lithium ion batteries, J. Mater. Chem. A 5 (18) (2017) 8762–8768.
[65] J. Zhang, L. Xu, C. Yang, X. Zhang, L. Ma, M. Zhang, J. Lu, Two-dimensional single-layer PC_6 as promising anode materials for Li-ion batteries: the first-principles calculations study, Appl. Surf. Sci. (2020) 145493.
[66] J.M. Tarascon, M. Armand, Issues and challenges facing rechargeable lithium batteries, Nature 414 (6861) (2001) 359–367.
[67] K. Toyoura, Y. Koyama, A. Kuwabara, F. Oba, I. Tanaka, First-principles approach to chemical diffusion of lithium atoms in a graphite intercalation compound, Phys. Rev. B 78 (21) (2008) 214303.
[68] X. Fan, W.T. Zheng, J.L. Kuo, Adsorption and diffusion of Li on pristine and defective graphene, ACS Appl. Mater. Interfaces 4 (5) (2012) 2432–2438.
[69] Ç. Girit, et al., Graphene at the edge: stability and dynamics, Science 323 (5922) (2009).
[70] H. Huang, H. Wu, C. Chi, J. Zhu, B. Huang, T. Zhang, Out-of-Plane ion transport makes nitrogenated holey graphite a promising high-rate anode for both Li and Na ion batteries, Nanoscale 11 (40) (2019) 18758–18768.
[71] D.H. Wu, B.C. Yang, H.Y. Chen, E. Ruckenstein, Nitrogenated holey graphene C_2N monolayer anodes for lithium- and sodium-ion batteries with high performance, Energy Storage Mater 16 (2019) 574–580.
[72] J. Liu, S. Wang, Q. Sun, All-carbon-based porous topological semimetal for Li-ion battery anode material, P. Natl. Acad. Sci. USA. 114 (4) (2017) 651–656.
[73] J. Liu, S. Wang, Y. Qie, C. Zhang, Q. Sun, High-pressure-assisted design of porous topological semimetal carbon for Li-ion battery anode with high-rate performance, Phys. Rev. Mater. 2 (2) (2018), 025403.
[74] Y. Jing, Z. Zhou, C. Cabrera, Z. Chen, Metallic VS_2 monolayer: a promising 2D anode material for lithium ion batteries, J. Phys. Chem. C 117 (48) (2013) 25409–25413.
[75] M. Koudriachova, N. Harrison, S.D. Leeuw, Open circuit voltage profile for Li-intercalation in rutile and anatase from first principles, Solid State Ionics 152 (2002) 189–194.
[76] W. Li, Y. Yang, G. Zhang, Y. Zhang, Ultrafast and directional diffusion of lithium in phosphorene for high-performance lithium-ion battery, Nano Lett. 15 (3)

(2015) 1691–1697.
[77] C. Eames, M.S. Islam, Ion intercalation into two-dimensional transition-metal carbides: global screening for new high-capacity battery materials, J. Am. Chem. Soc. 136 (2014) 16270–16276.
[78] C.K. Chan, H. Peng, G. Liu, K. McIlwrath, X.F. Zhang, R.A. Huggins, Y. Cui, High-performance lithium battery anodes using silicon nanowires, Nat. Nanotechnol. 3 (1) (2008) 31–35.
[79] J. Su, T. Duan, W. Li, B. Xiao, G. Zhou, Y. Pei, X. Wang, A first-principles study of 2D antimonene electrodes for Li ion storage, Appl. Surf. Sci. 462 (2018) 270–275.
[80] J. Bai, X. Zhong, S. Jiang, Y. Huang, X. Duan, Graphene Nanomesh. *Nat. Nanotechnol.* 5 (3) (2010) 190.
[81] Y. Yang, X. Yang, L. Liang, Y. Gao, H. Cheng, X. Li, M. Zou, R. Ma, Q. Yuan, X. Duan, Large-area graphene-nanomesh/carbon-nanotube hybrid membranes for ionic and molecular nanofiltration, Science 364 (6445) (2019) 1057–1062.